CHAPTER IV

RESULT AND DISCUSSION

4.1 Base Case Analysis

For the base case reservoir properties, the result from ECLIPSE simulation of gas production and reservoir pressure is shown in Fig.4.1. The well was set to produce oil at a constant rate of 1,000 BOPD throughout the well's life. In the base case which has the bubble point pressure of 2,000 psi, the reservoir pressure, initially at 3,000 psi, rapidly decreases because of no existing free gas and aquifer. The only source of material replacing the produced fluid is the expansion of oil remaining in the reservoir. The gas which is produced at a constant rate of around 450 Mscf/d when the pressure is above the bubble point pressure comes from solution gas.

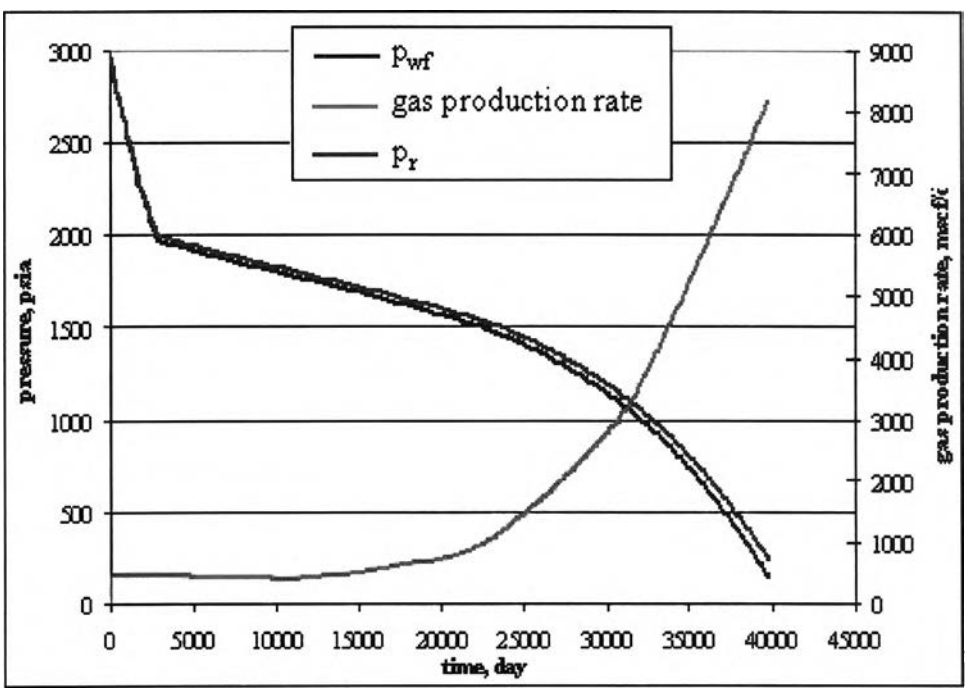

Figure 4.1: Gas production, reservoir pressure, and well flowing pressure profile.

When the reservoir pressure decreases below the bubble point pressure of 2,000 psi, free gas is available and able to expand to replace the produced fluid. The reservoir pressure then gradually decreases. The gas production slightly decreases for a while since the amount of free gas is not large enough for it to be movable. When the reservoir pressure decreases from 2,000 to 1,760 psi, the gas production decreases from 450 to 410 Mscf/d. However, as soon as the gas saturation exceeds the critical gas saturation, the gas production rapidly increases as the reservoir pressure decreases as shown in Fig 4.1. The gas production increases from 800 Mscf/d to 7,800 Mscf/d.

Modified isochronal plots were simulated for different stages of depletion to estimate flow exponent, n, and PI coefficient, J at each depletion stage. The parameters J and n for each depletion stage were calculated by fitting a straight line to the log-log plot using regression. Fig 4.2 is an example of the log-log plot when the reservoir pressure is 2,000 and 1,027 psia at two depletion stages. The value of J and n are 1.0224 and 88.2265×10^4, respectively, when the reservoir pressure is 2,000 psia and 1.0251 and 77.7693×10^4, respectively, when the reservoir pressure is 1,027 psia.

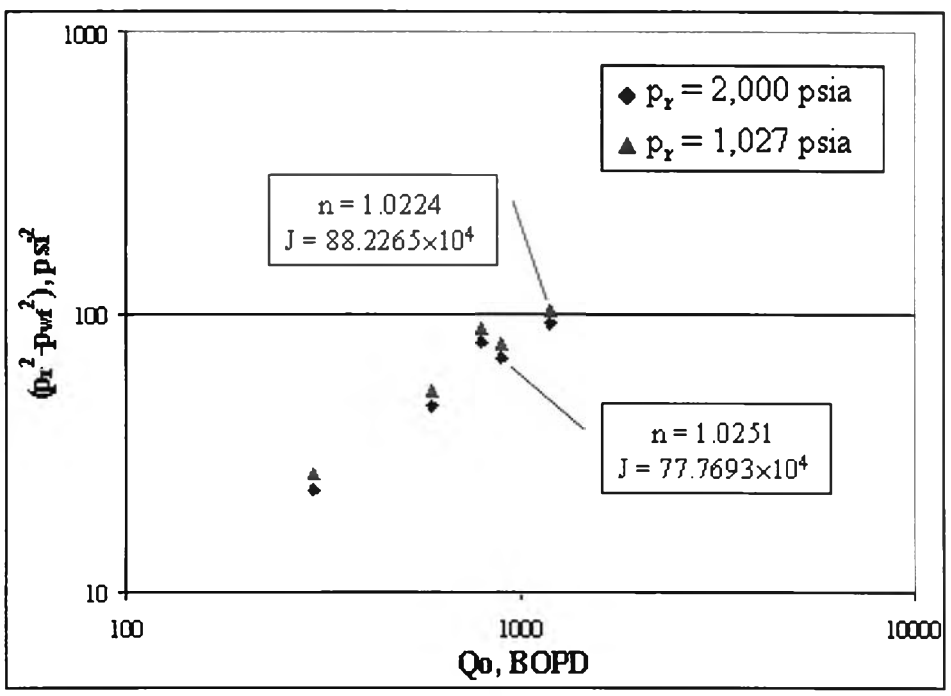

Figure 4.2: Flow constants J and n calculated with base-case reservoir data.

The values of the parameters n and J at each depletion stage for the base case are shown in Fig 4.3 and Fig 4.4. Below the bubble point pressure, as the pressure depletes, the value of n first slightly increases and then gradually decreases and later sharply increases. The first increase happens during the initial evolution of gas from the oil phase where the gas saturation is still lower than the critical value. When there is enough gas saturation, the gas starts to move. The value of J slightly decreases for some period and sharply increases at low pressures.

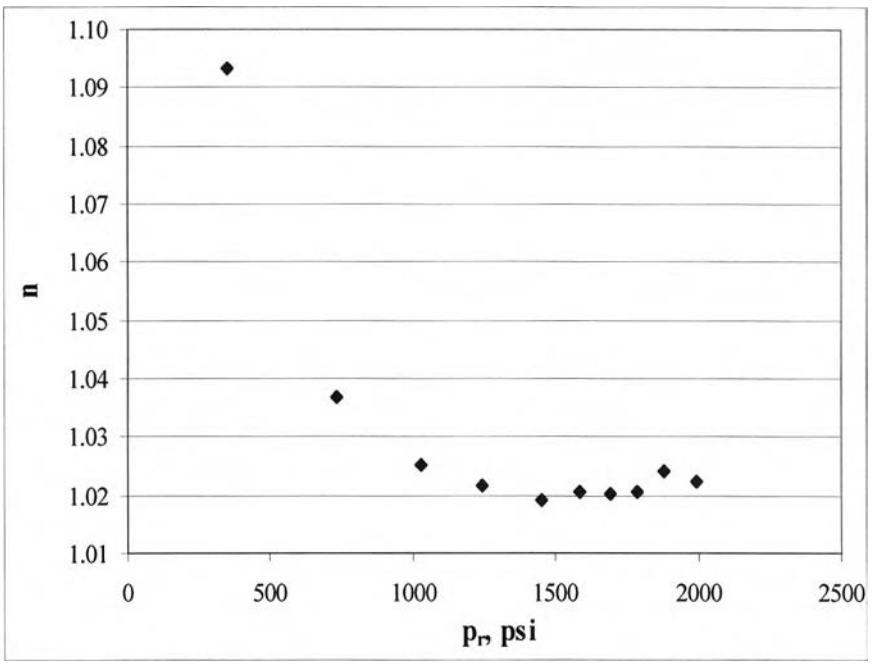

Figure 4.3: Base case flow exponent, n, with reservoir pressure.

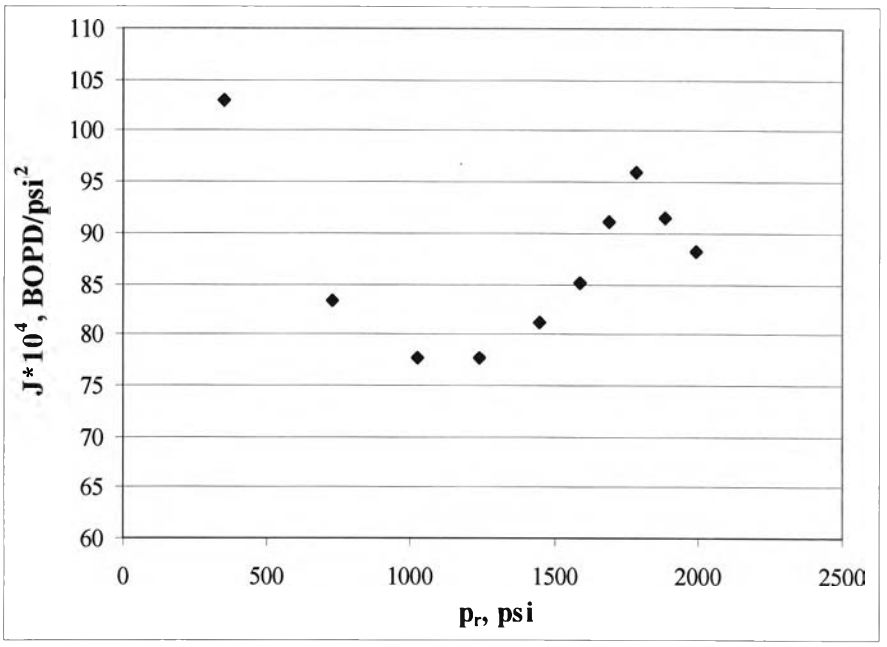

Figure 4.4: Base case PI coefficient, *J*, with reservoir pressure.

Below the bubble point, as the pressure depletes, the value of *J* increases for a short period and starts to fall down and increases again. During the initial period, parts of the oil evolve into free gas, and the free gas is still unmovable since its saturation is less than the critical gas saturation. As shown in Fig. 4.5, the gas production is constant above the bubble point pressure, indicating single phase oil flow, and slightly decreases when the pressure drops below 2,000 psi., indicating single phase oil flow with some unmovable free gas. When the gas saturation is above the critical value, gas starts to flow. The value of *J* starts to decrease and increase again.

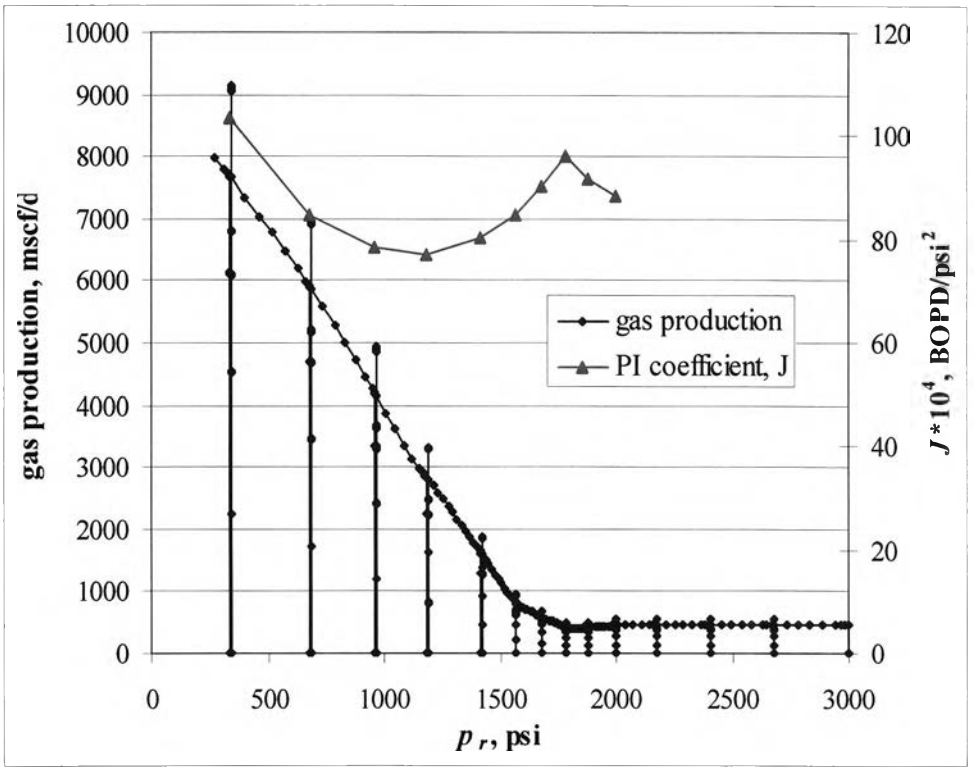

Figure 4.5: Base case PI coefficient, J, and gas production with reservoir pressure.

These parameters n and J were then normalized with n_b and J_b, the parameters determined at the bubble point pressure. The dimensionless value n/n_b and dimensionless value J/J_b as a function of dimensionless pressure, p_r/p_b are shown in Figs. 4.6 and 4.7.

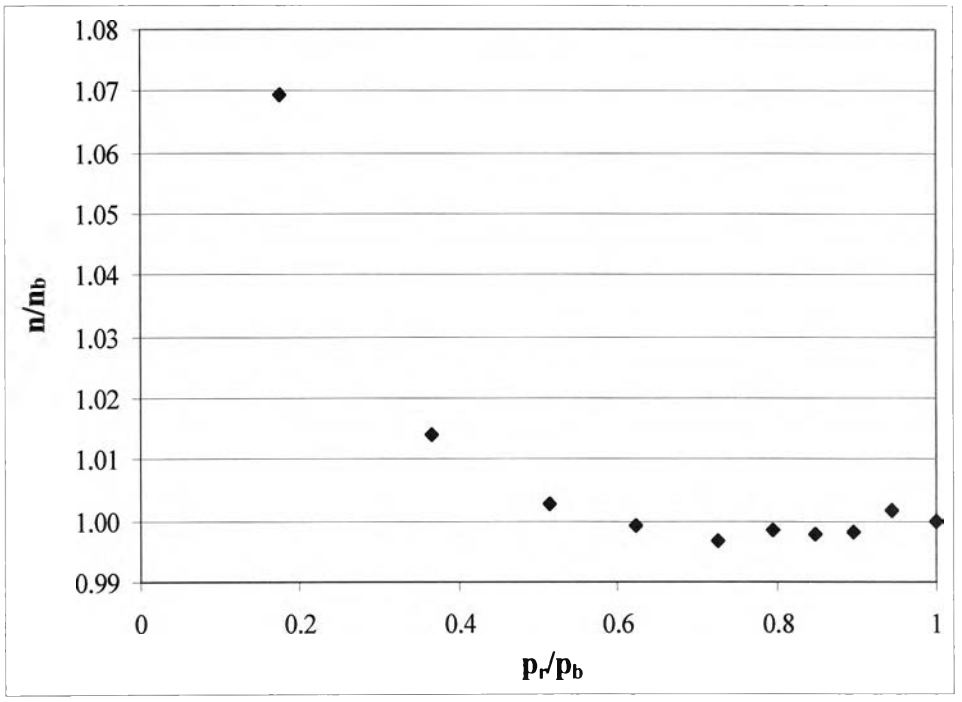

Figure 4.6: Base case dimensionless flow exponent, n/n_b, with dimensionless pressure, p_r/p_b.

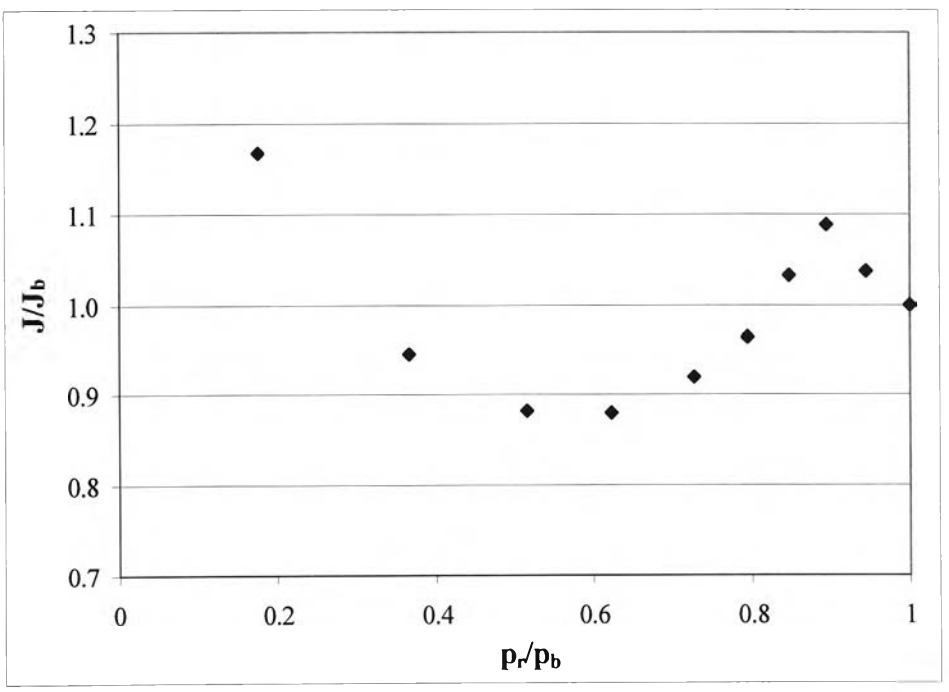

Figure 4.7: Base case dimensionless PI coefficient, J/J_b, with dimensionless pressure, p_r/p_b.

4.2 Effect of Changes in Reservoir and Fluid Properties

4.2.1. Effect of Drainage Area

In this study, the drainage area was varied from 150×150 to 250×250 and 350×350 ft^2. Fig. 4.8 shows the reservoir pressure for each case when oil is produced at 1,000 BOPD until the reservoir pressure is depleted. As seen in the figure, the bigger the drainage area, the slower the reservoir pressure decreases. This is due to the fact that a larger reserve has more oil, solution gas, and free gas to support the reservoir. As a result, the reservoir pressure depletes slower.

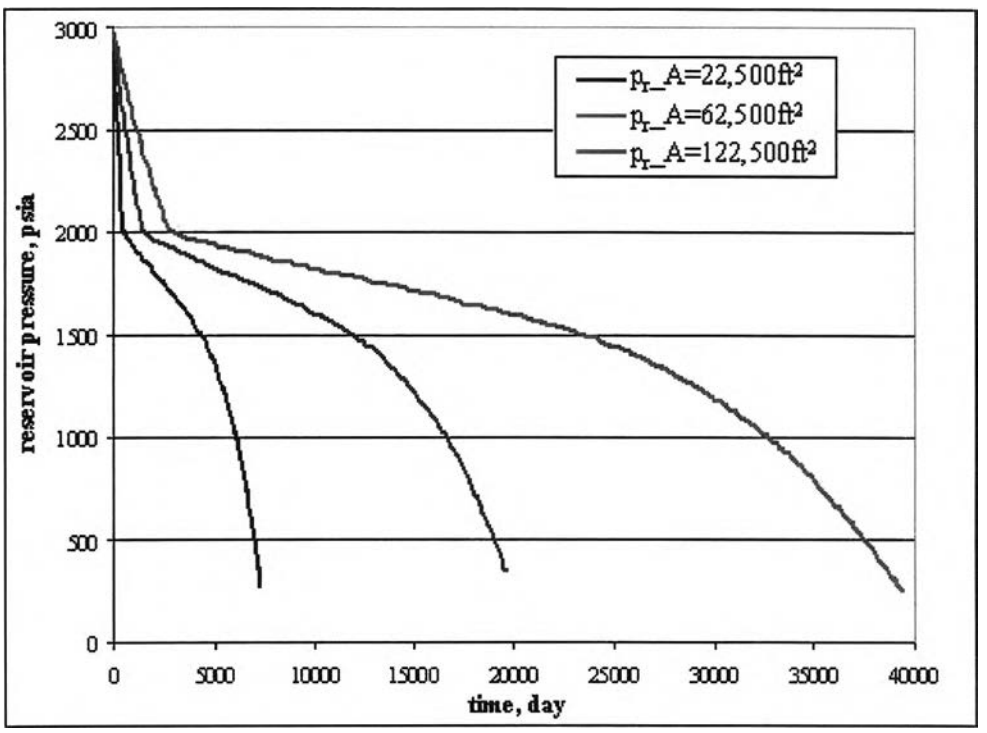

Figure 4.8: The decline of reservoir pressure for different sizes of drainage area.

Figs. 4.9 and 4.10 shows n and J values for different drainage areas as a function of reservoir pressure. The values of n and J do not change much as the drainage area changes.

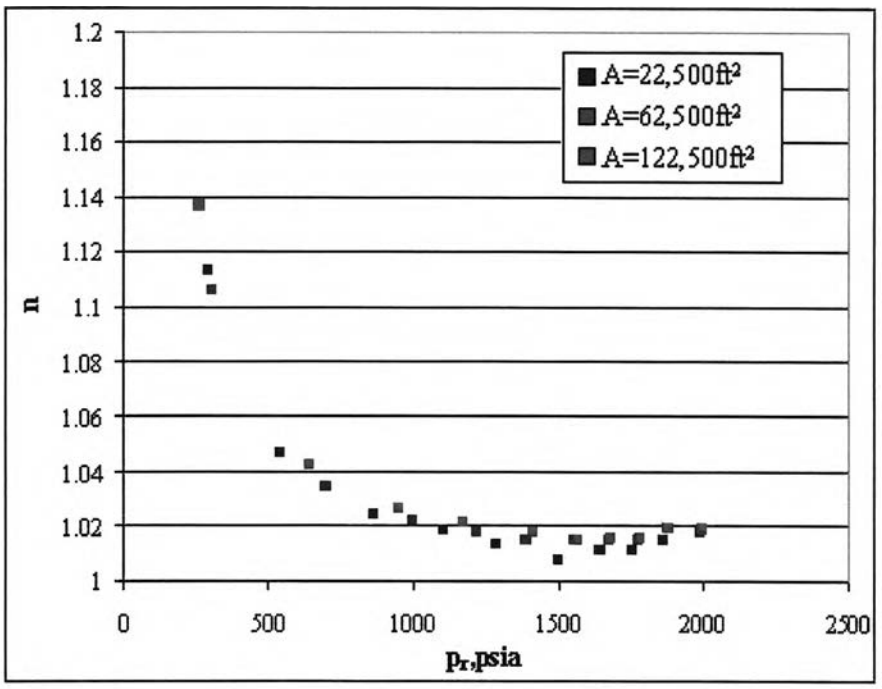

Figure 4.9: *n* value for different drainage areas as a function of reservoir pressure.

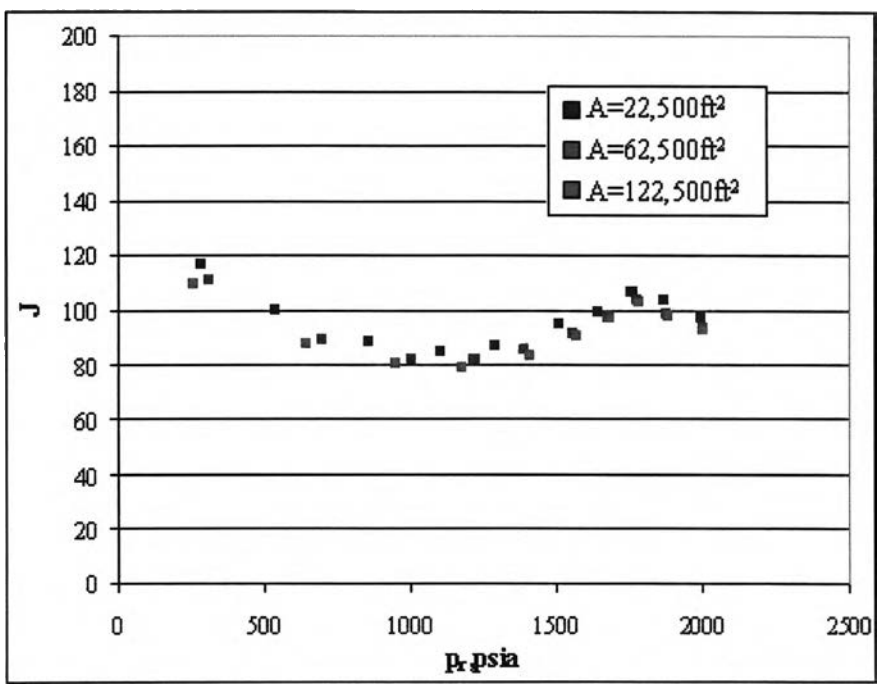

Figure 4.10: *J* value for different drainage areas as a function of reservoir pressure.

4.2.2 Effect of Permeability

In this study, permeability was varied using 3 values. Case A has permeability of 50 md.; Case B has permeability of 250 md; and Case C has permeability of 1,000 md. Others parameters were base case parameters. From the simulation runs, the difference between flowing bottomhole pressure and reservoir pressure for the case which has the lowest value of permeability, 50 md, was the largest. This behavior corresponds with Darcy's law which states that lower permeability induces high pressure drop. For the cases which have the permeability of 250 and 1,000 md, the differences between flowing bottomhole pressure and reservoir pressure are almost the same. Figs. 4.12 and 4.13 show n and J values for various permeabilites. When the reservoir pressure decreases below 1,500 psia, n value becomes very high for the reservoir that has a permeability of 50 md. The value of J increases with increased permeability which corresponds with Fetkovich's equation that with lower difference between reservoir pressure and flowing bottomhole pressure, J value will be larger.

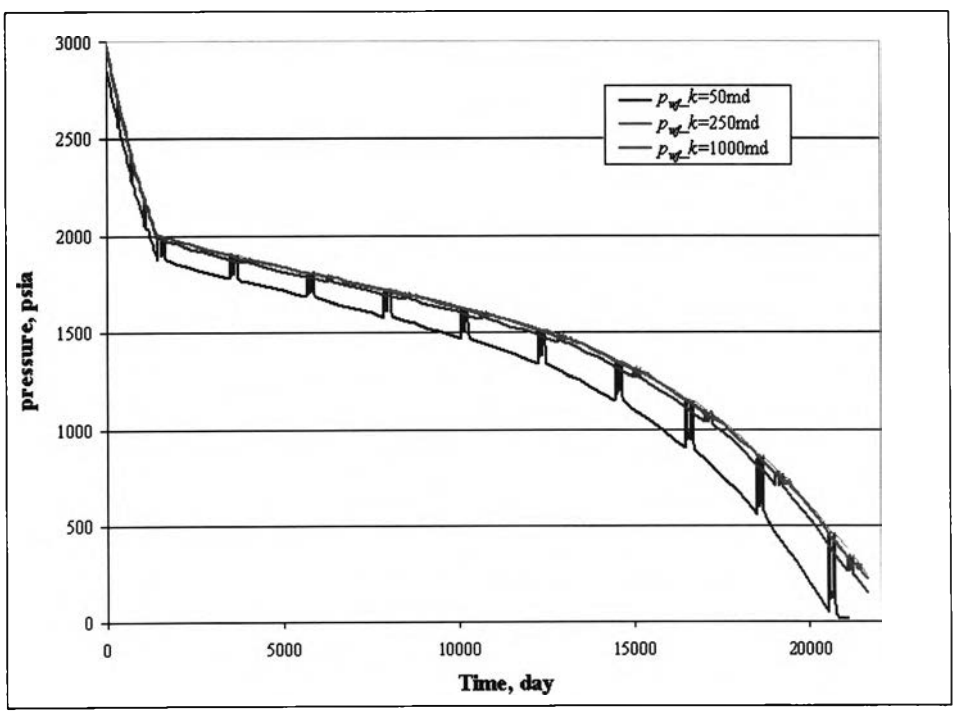

Figure 4.11: Reservoir pressure and gas production as a function of time for different permeability values.

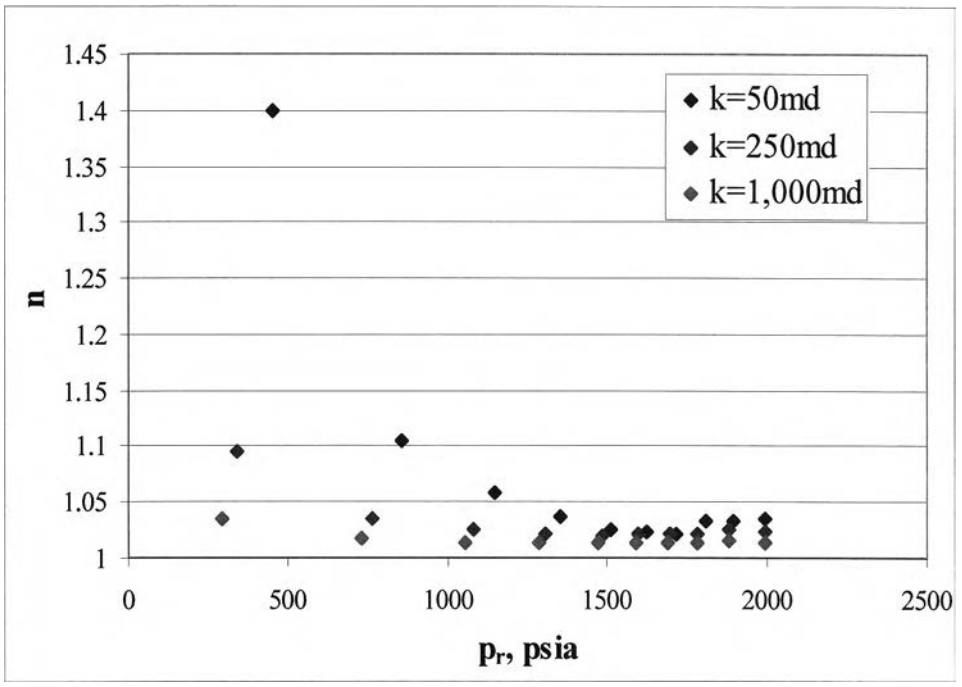

Figure 4.12: *n* value for different permeabilities as a function of reservoir pressure.

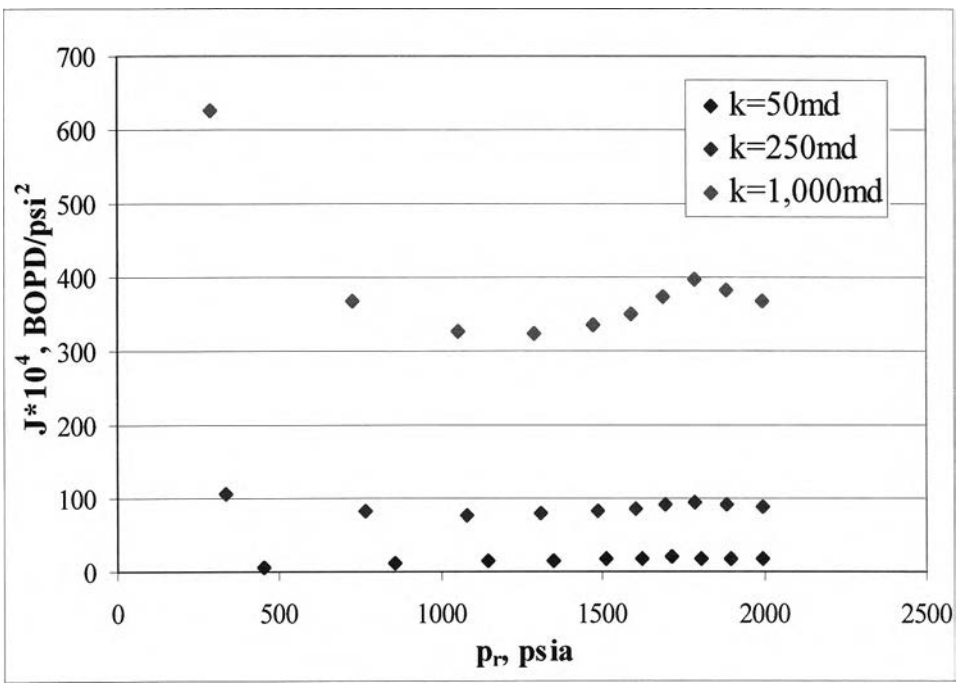

Figure 4.13: *J* value for different permeabilities as a function of reservoir pressure.

4.2.3 Effect of Porosity

To study the effect of porosity, 3 values of porosity were used in the study. Case A has a porosity of 0.10; Case B has a porosity of 0.15; and Case C has a porosity of 0.20. The results from the simulation show that the higher the porosity, the slower the reservoir pressure will decline. This behavior is shown in Fig. 4.14. The value of n and J are shown in Fig. 4.15 and Fig. 4.16. The difference in porosity value does not significantly alter the values of n and J.

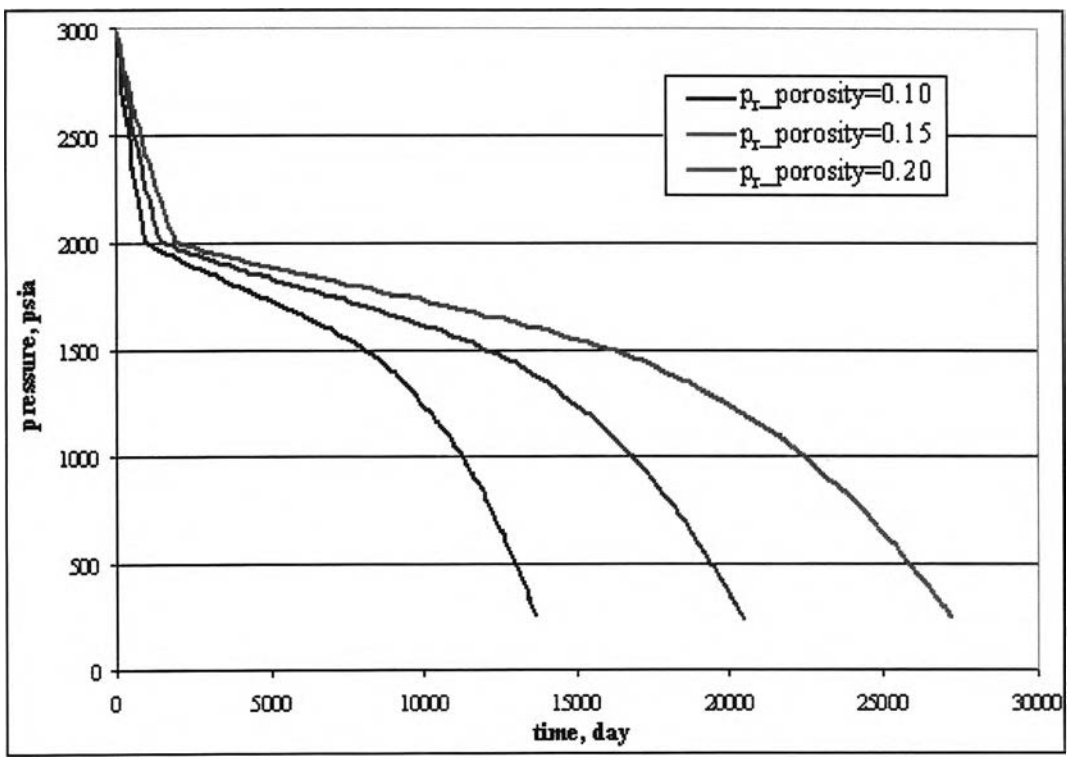

Figure 4.14: Reservoir pressure and gas production as a function of time for different porosity values.

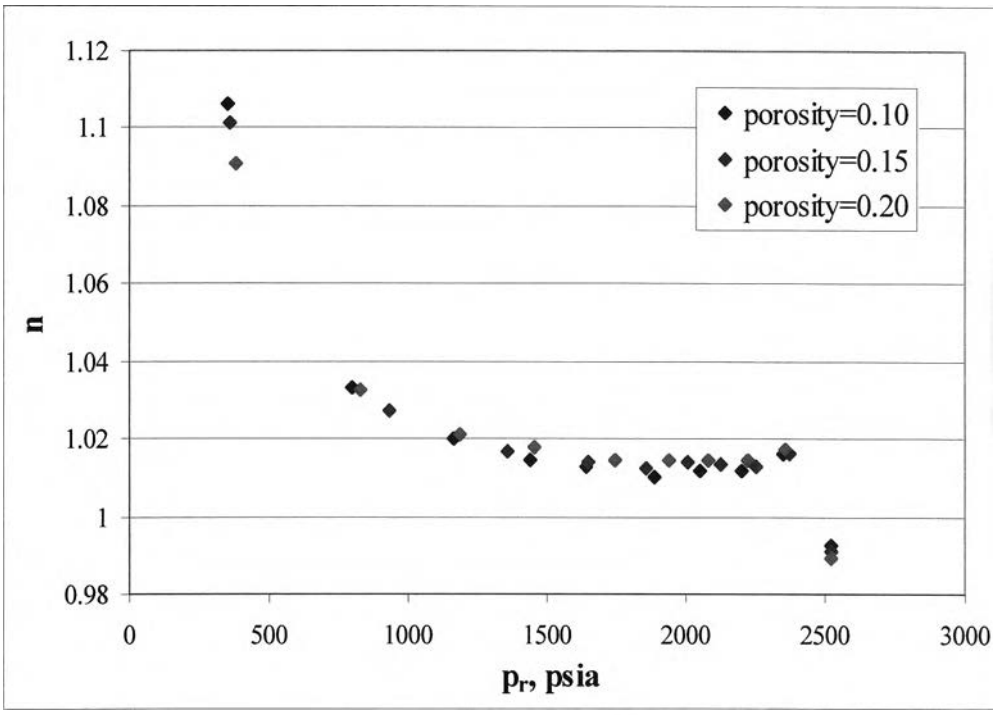

Figure 4.15: *n* value for different porosities as a function of reservoir pressure.

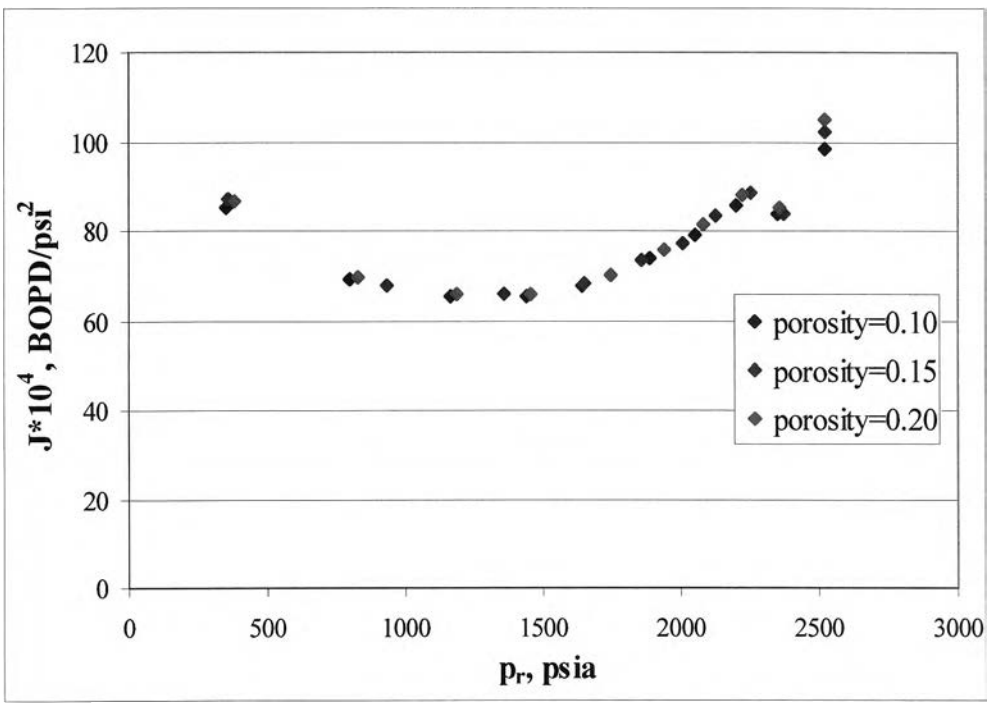

Figure 4.16: *J* value for different porosities as a function of reservoir pressure.

4.2.4 Effect of Bubble Point Pressure

In this study, three values of bubble point pressure were used. Case A has the bubble point pressure of 1,500 psia; Case B has the bubble point pressure of 2,000 psia; and Case C has the bubble point pressure of 2,500 psia. From the result shown in Fig. 4.17, the higher the bubble point pressure, the higher the gas production and the faster the reservoir pressure depletes. This is due to the fact that gas comes out of solution faster than the bubble point pressure is high. The faster gas evolves out of oil, the faster the pressure depletes.

The values of n and J from modified isochronal test with varying bubble point pressures are shown in Figs. 4.18 and 4.19. The trends of n values for different bubble point pressures look the same but the value of J for a reservoir with a lower bubble point pressure is higher.

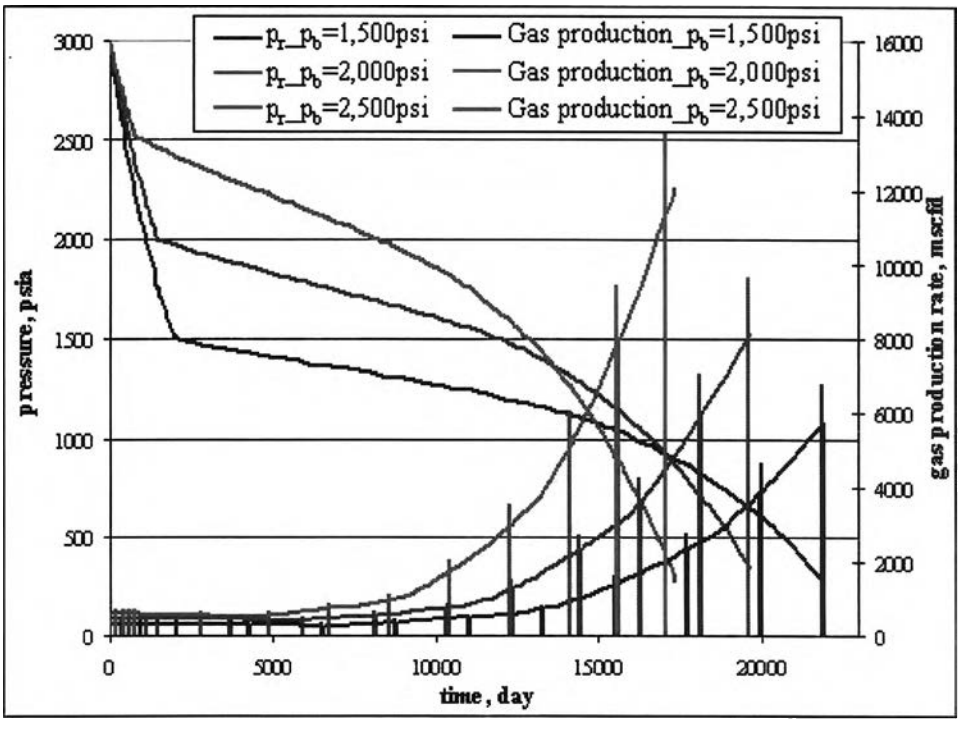

Figure 4.17: Reservoir pressure and gas production as a function of time for different bubble pressure values.

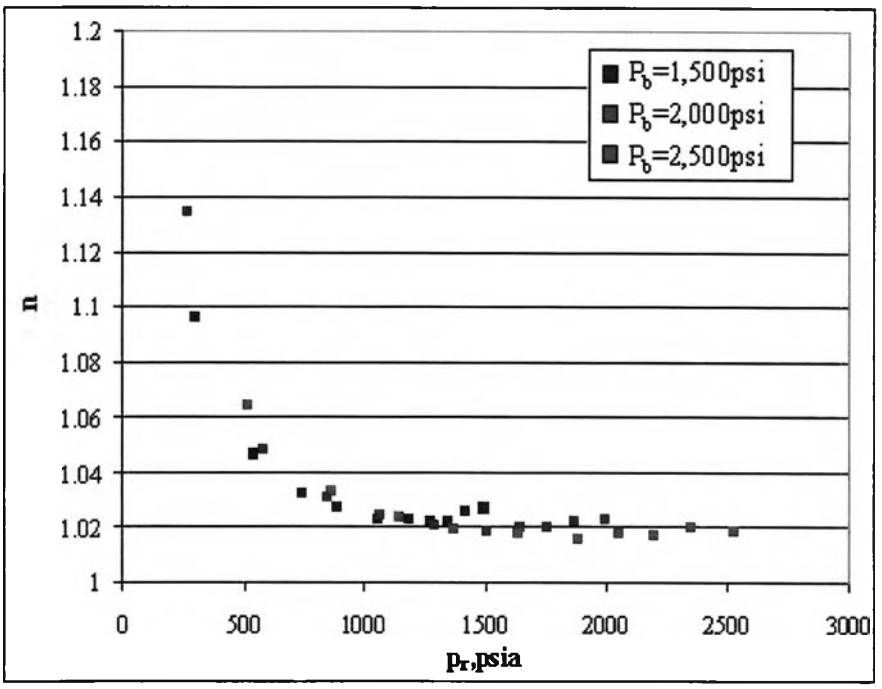

Figure 4.18: *n* value for different bubble point pressures as a function of reservoir pressure.

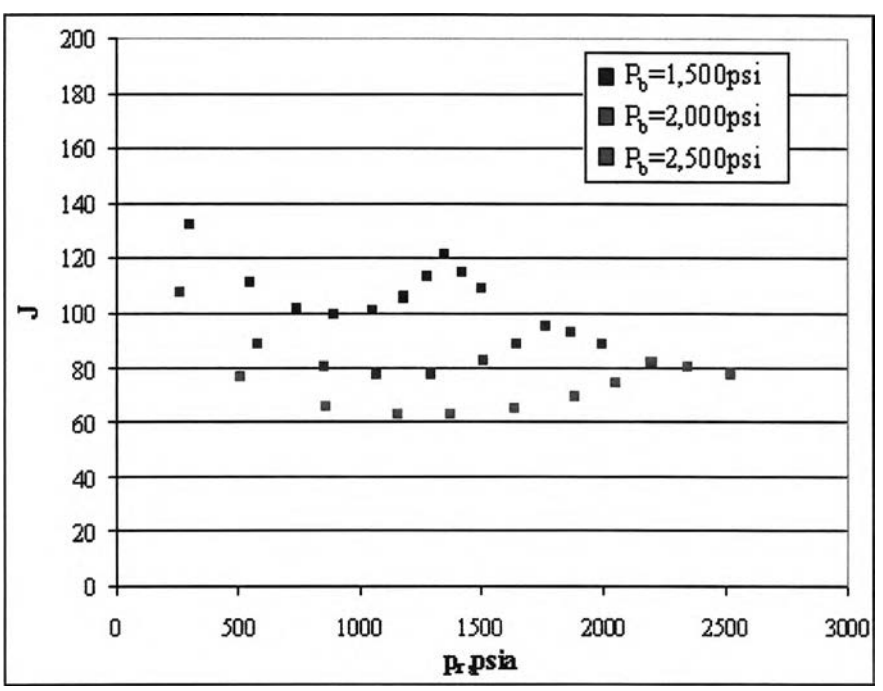

Figure 4.19: *J* value for different bubble point pressures as a function of reservoir pressure.

4.2.5 Effect of Critical Gas Saturation

The critical gas saturation, S_{gc}, was varied from 0.0 to 0.1 and 0.2 in case A, case B, and case C, respectively. The saturation function with relative permeability is shown in Figs. 3.1, 3.2, and 3.3. From the result shown in Fig. 4.20, at lowest S_{gc}, the gas production is the highest. The reservoir pressure for this case depletes the fastest because there is less gas to expand to support produced liquid. Figs. 4.21 and 4.22 show the relationship of n and J value for different reservoir pressures.

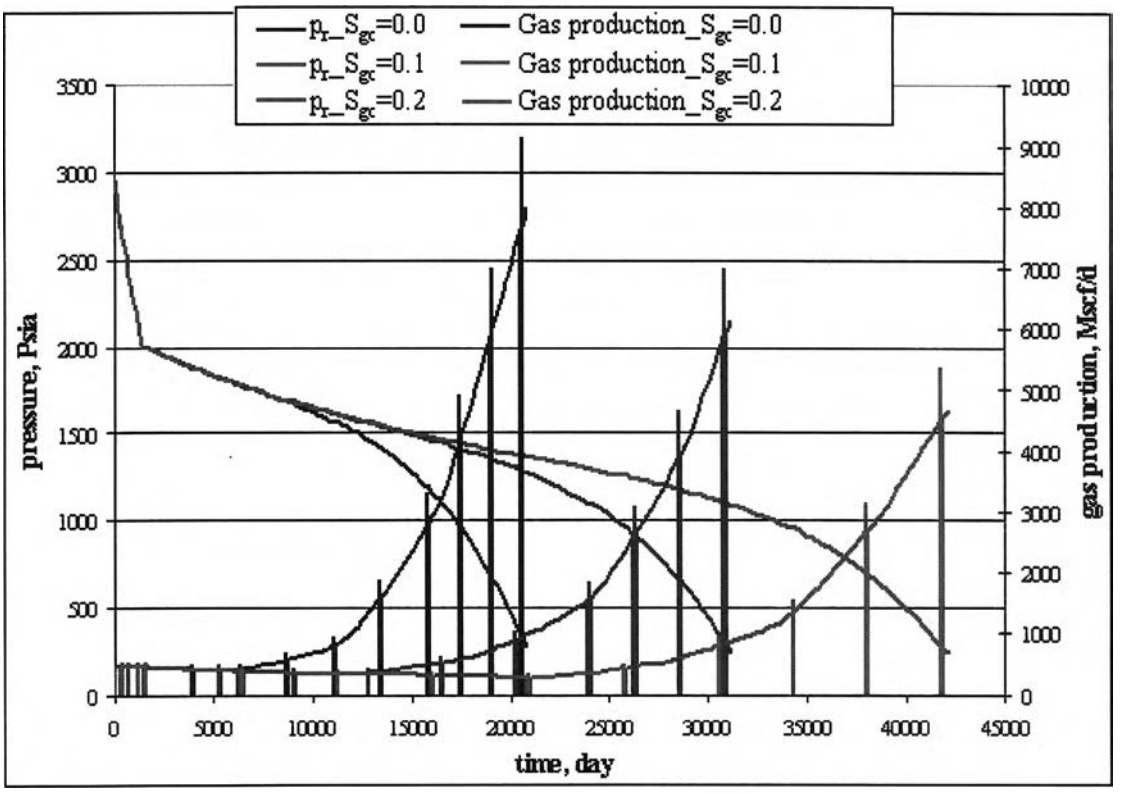

Figure 4.20: Reservoir pressure and gas production as a function of time for different critical gas saturation values.

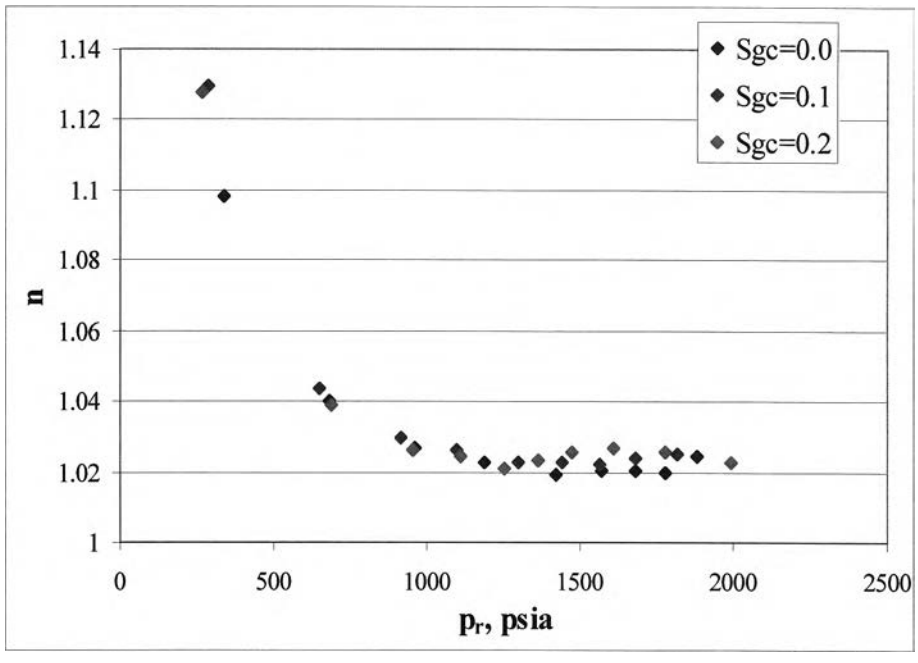

Figure 4.21: *n* value for different critical gas saturations as a function of reservoir pressure.

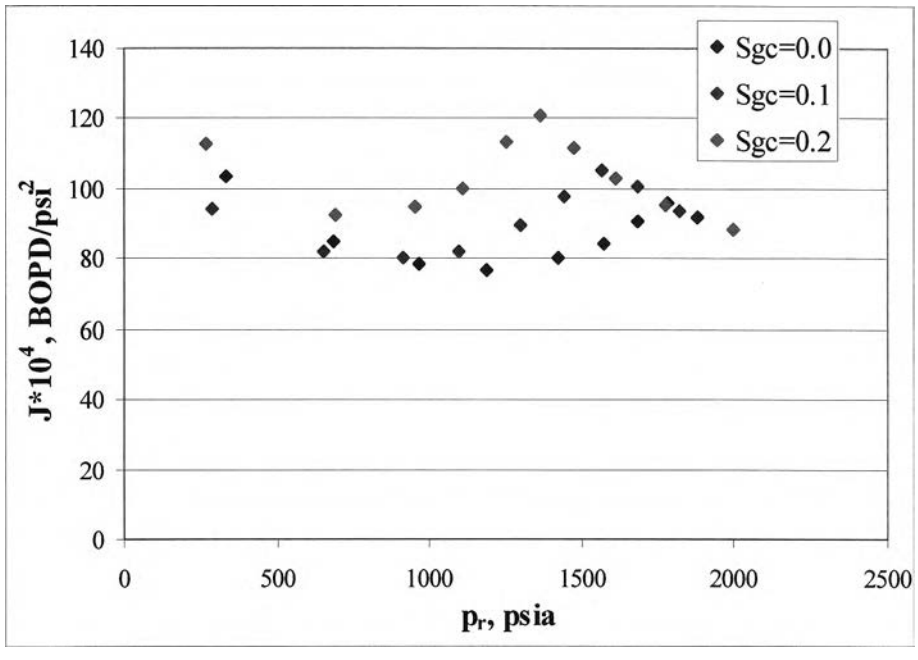

Figure 4.22: *J* value for different critical gas saturations as a function of reservoir pressure.

4.3 Determination of Empirical Correlations for Future IPR

With eighty-one cases of reservoir simulation, the relationship of dimensionless flow exponent n/n_b and dimensionless pressure, p_r/p_b, is shown in Fig. 4.23. Fig. 4.24 shows the relationship of dimensionless J/J_b to the dimensionless pressure p_r/p_b. In these figures, the values of n/n_b and J/J_b during the first period where the free gas is still unmovable are omitted from the plot. The tail of each curve is excluded in order to avoid mixing different trends in the same graph. The value of dimensionless flow exponent n/n_b is almost constant when p_r/p_b is between 0.5 - 1.0 but increases as p_r/p_b becomes lower while J/J_b decreases when p_r/p_b is decreased from 1.0 to 0.5 but increases as p_r/p_b becomes lower as a result of larger amount of gas production.

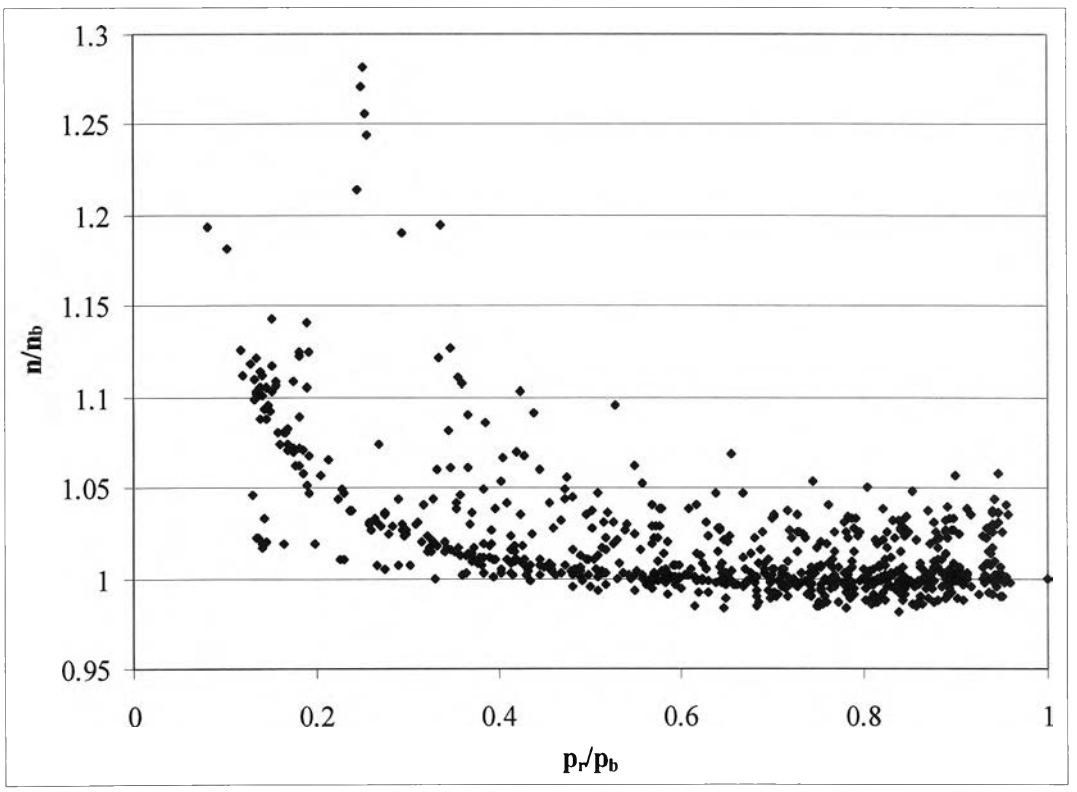

Figure 4.23: Dimensionless flow exponent, n/n_b, as a function of dimensionless pressure, p_r/p_b.

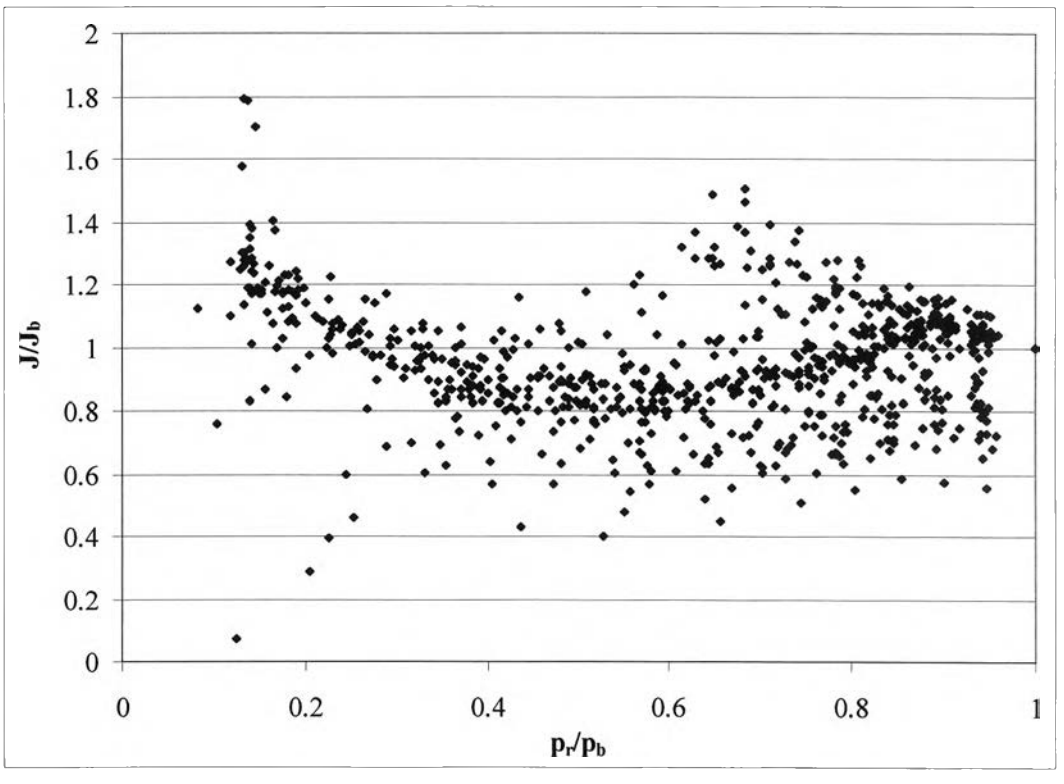

Figure 4.24: Dimensionless flow constant, J/J_b, as a function of dimensionless pressure, p_r/p_b.

Polynomial equations were used to fit these data in order to determine empirical correlations for dimensionless n/n_b and J/J_b to dimensionless p_r/p_b. The first, second, third, and fourth-order polynomial equations were tried. The results of the fit are shown in Figs. 4.25, 4.26, 4.27, and 4.28.

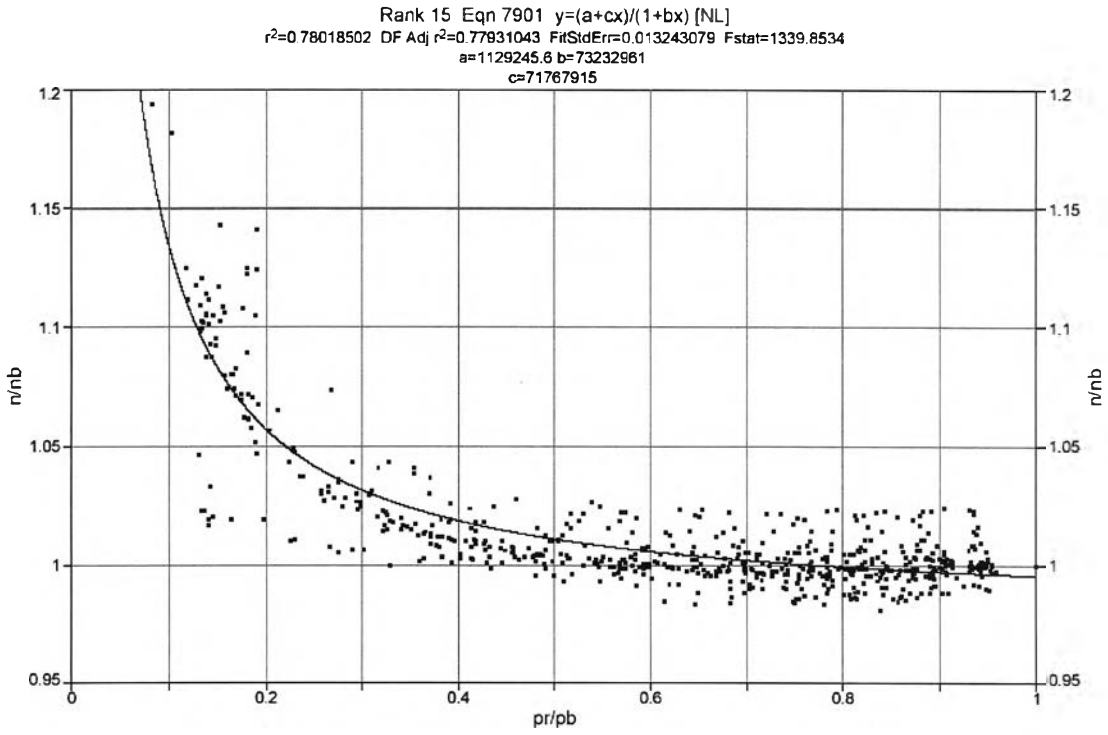

Figure 4.25: A first-order polynomial fit for the relationship of n/n_b vs. p_r/p_b.

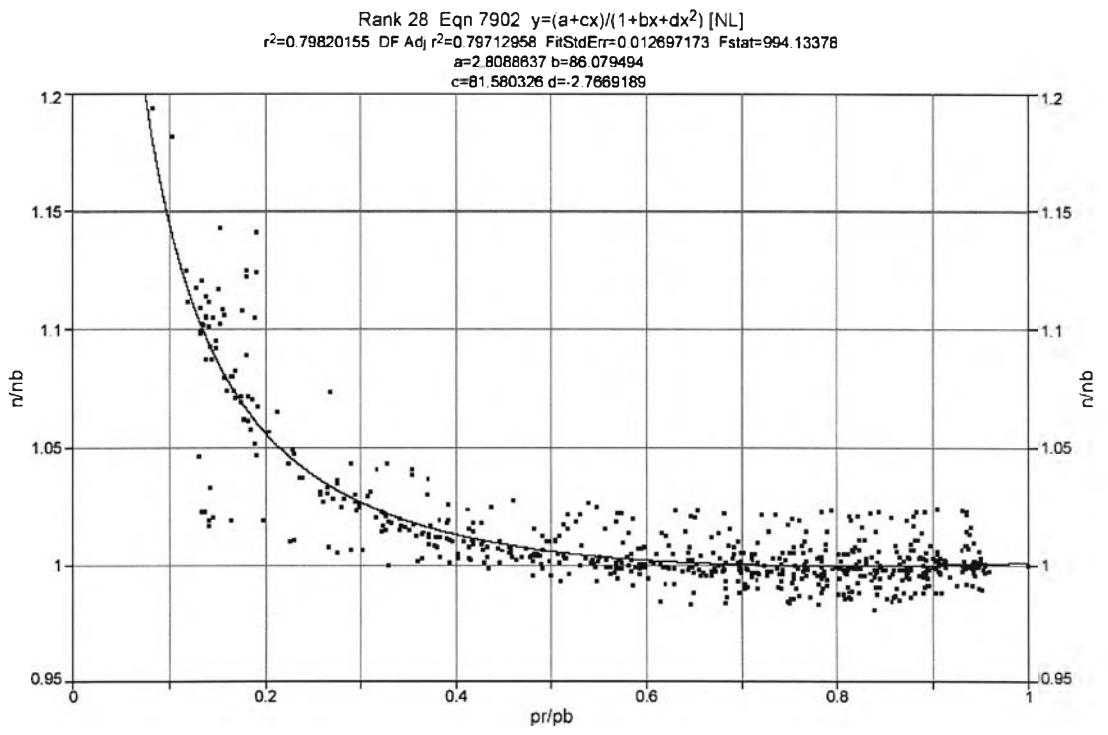

Figure 4.26: A second-order polynomial fit for the relationship of n/n_b vs. p_r/p_b.

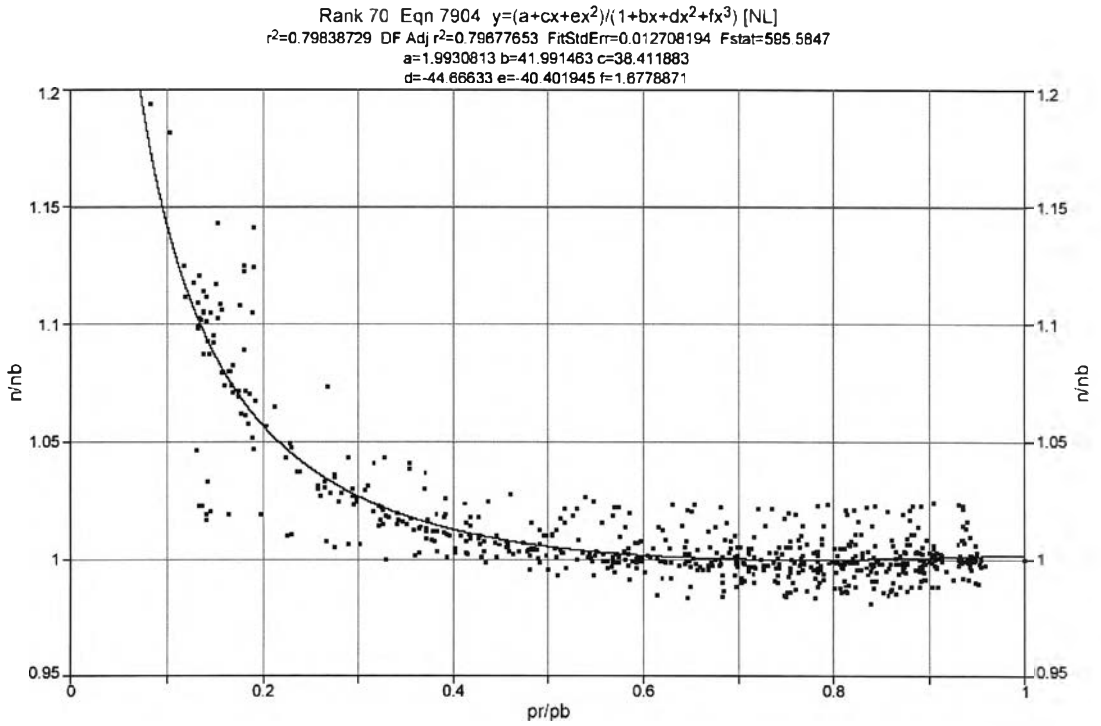

Figure 4.27: A third-order polynomial fit for the relationship of n/n_b vs. p_r/p_b.

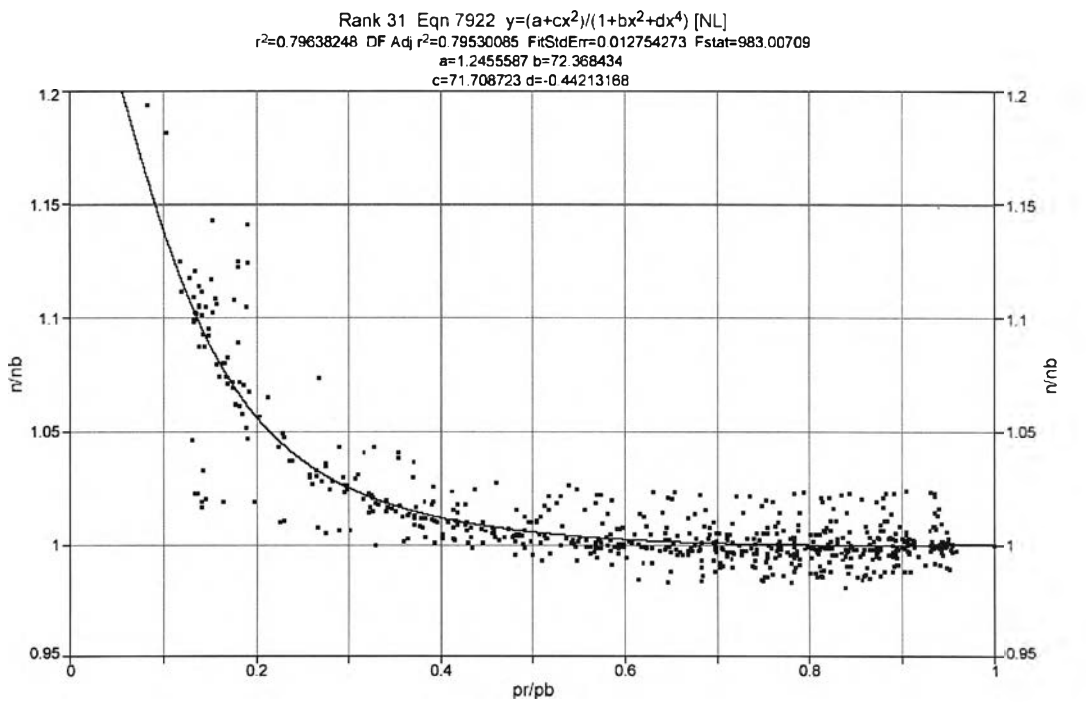

Figure 4.28: A fourth-order polynomial fit for the relationship of n/n_b vs. p_r/p_b.

The first, second, third, and fourth-order polynomials give the value of R^2 equal to 0.7801, 0.7962, 0.7963, and 0.7964, respectively. The R-squared value is the relative predictive power of a model and is a descriptive measure between 0 and 1. The closer it is to one, the better the model is. According to this criteria, the fourth-order model should be the equation. However, the second-order polynomial was chosen as the empirical equation to describe the relationship between dimensionless n/n_b vs. p_r/p_b since the fourth-order polynomial gives a slightly higher R-square, R^2, value but the second-order polynomial is less complicated.

First, second, third, and fourth-order polynomial equations were also used to determine the empirical correlation of the relationship of dimensionless J/J_b and p_r/p_b as shown in Figs. 4.29, 4.30, 4.31, and 4.32.

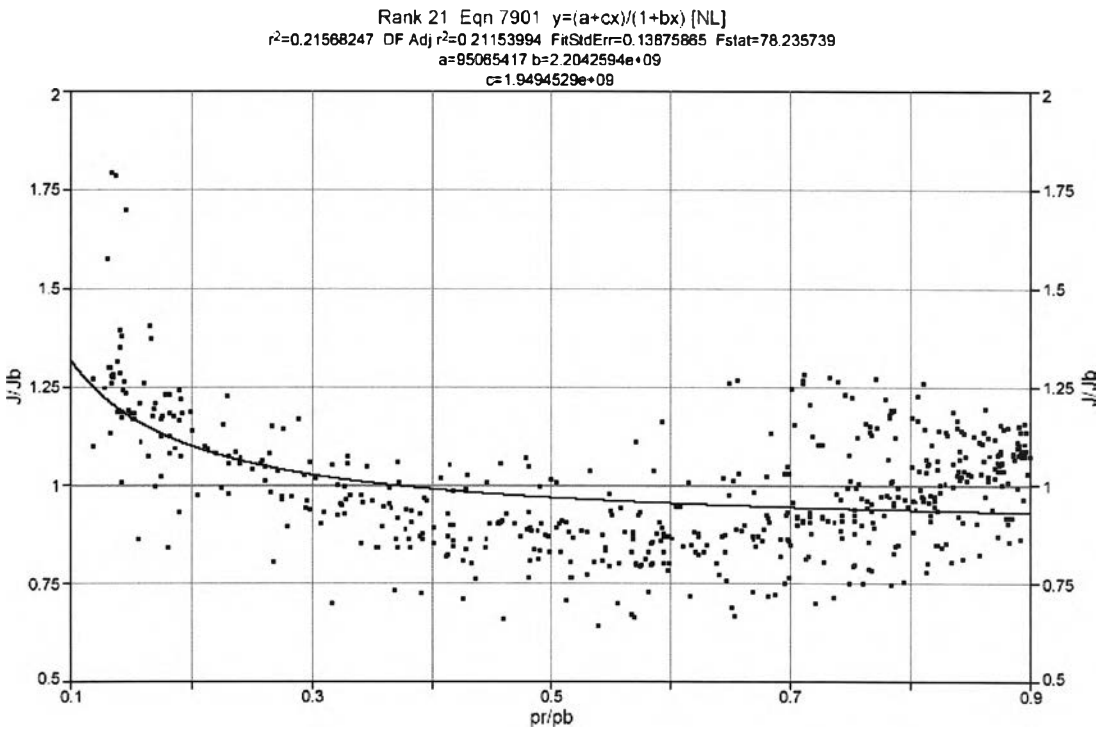

Figure 4.29: A first-order polynomial fit for the relationship of J/J_b vs. p_r/p_b.

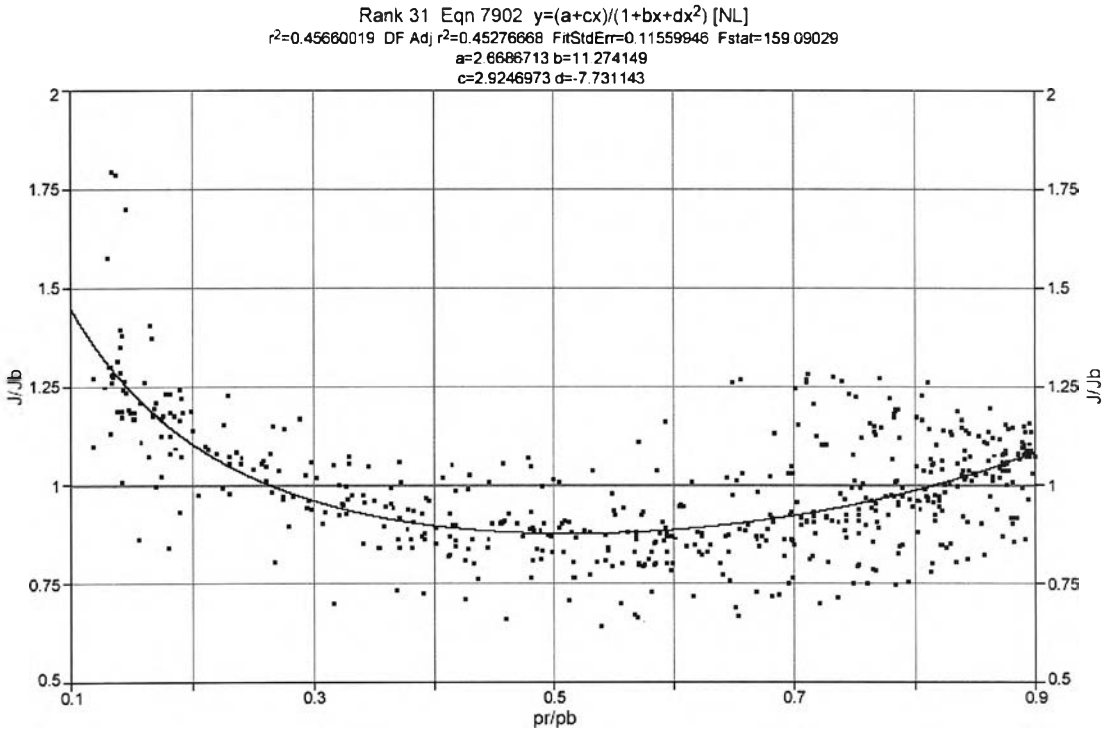

Figure 4.30: A second-order polynomial fit for the relationship of J/J_b vs. p_r/p_b.

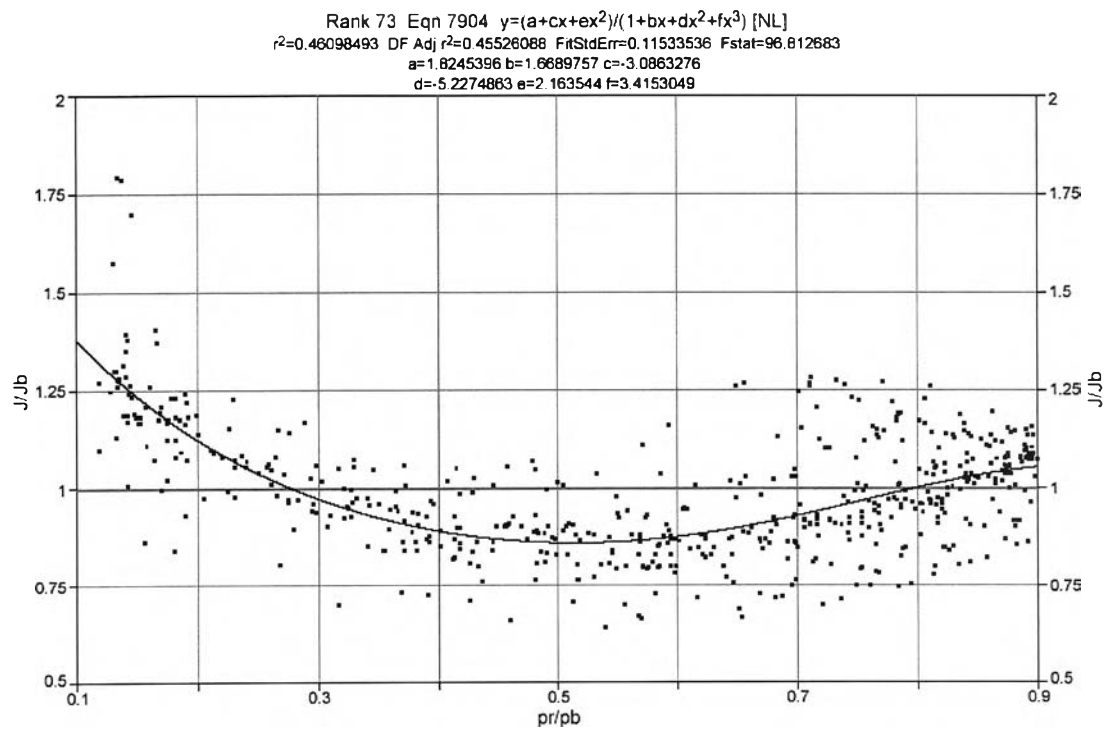

Figure 4.31: A third-order polynomial fit for the relationship of J/J_b vs. p_r/p_b.

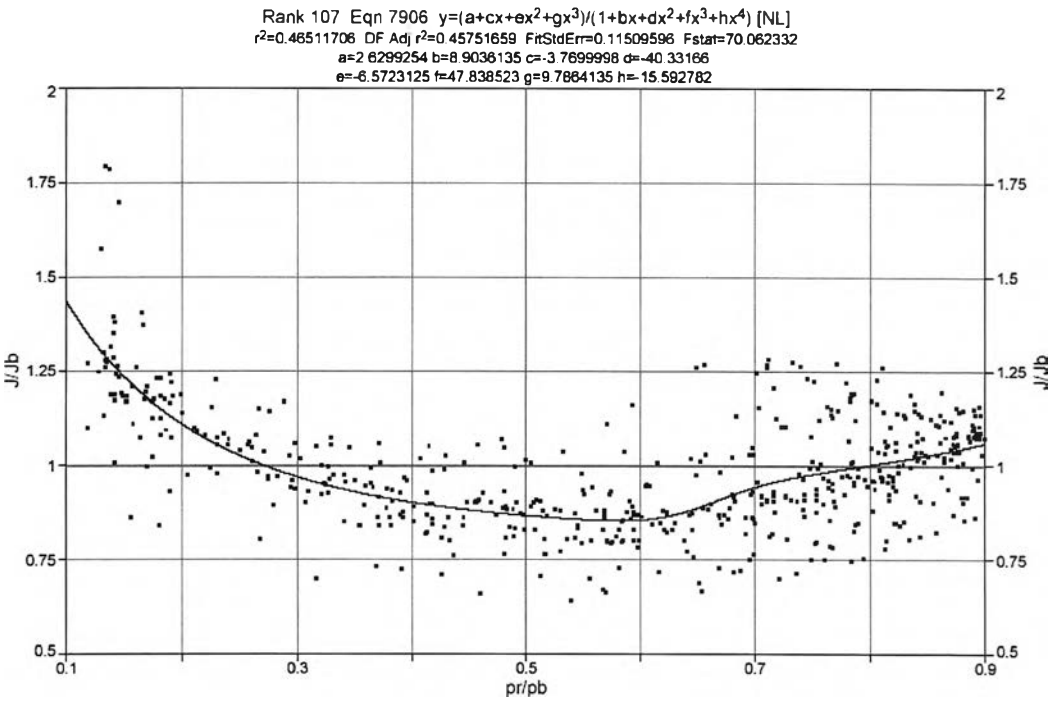

Figure 4.32: A fourth-order polynomial fit for the relationship of J/J_b vs. p_r/p_b.

The first, second, third, and fourth-order polynomials give the value of R^2 equal to 0.2157, 0.4566, 0.4609, and 0.4651, respectively. The second-order polynomial was chosen the most suitable fit for the dimensionless J/J_b vs. p_r/p_b due to its simplicity although its R^2 value is slightly less than that of the fourth-order polynomial. Another reason for not choosing the fourth-order model is that the fourth-order equation does not provide a smooth fit when the dimensionless p_r/p_b equals to 0.65-0.75.

In summary, the equations that were chosen for dimensionless n/n_b and J/J_b are

$$\frac{n}{n_b} = \frac{2.8089 + 81.5803\left(\frac{p_r}{p_b}\right)}{1 + 86.0795\left(\frac{p_r}{p_b}\right) - 2.7669\left(\frac{p_r}{p_b}\right)^2} \qquad [4.1]$$

and

$$\frac{J}{J_b} = \frac{2.6687 + 2.9247\left(\frac{p_r}{p_b}\right)}{1 + 11.2741\left(\frac{p_r}{p_b}\right) - 7.7311\left(\frac{p_r}{p_b}\right)^2} \qquad [4.2]$$

With these two equations, n and J can be estimated at any reservoir pressure to predict future inflow performance relationship. An example of this calculation is given later in section 4.4.

The curve of exponent (n) generally exhibits about the same shape except some cases which give a different shape as shown in Fig 4.33. These cases occur when

- p_b = 1,500 psia, permeability = 50 md.
- p_b = 2,000 psia, permeability = 50 md.
- p_b = 2,500 psia, permeability = 50 md.

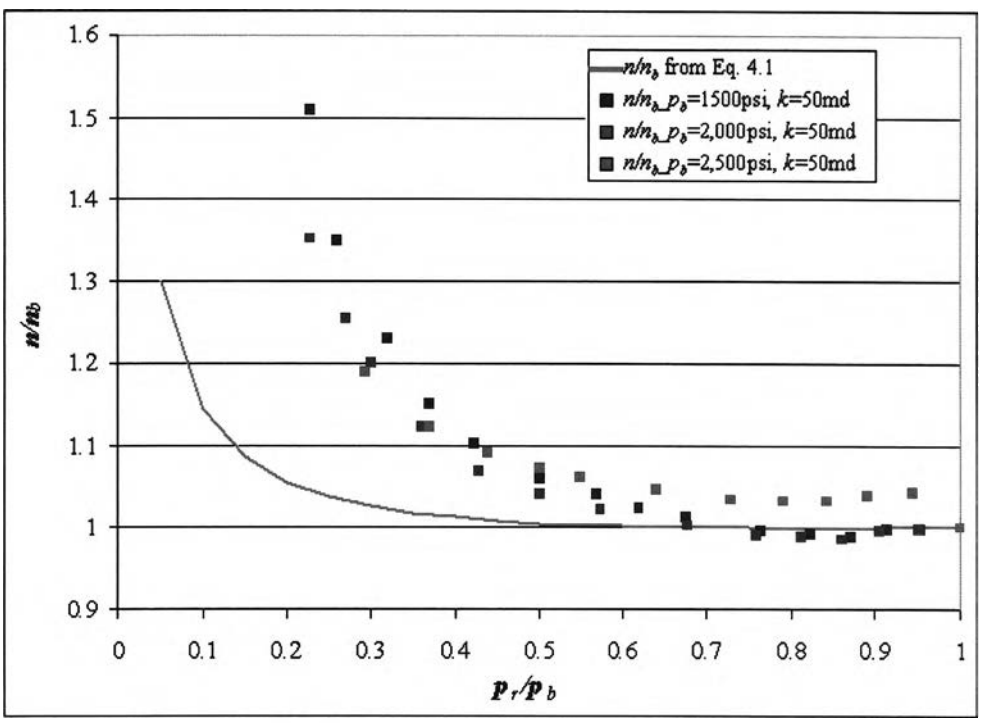

Figure 4.33: n/n_b value as a function of p_r/p_b which has different shape from calculation value of n/n_b.

The curve of PI exponent (J) generally exhibits the same shape except some cases which give a different shape as shown in Fig. 4.34. These cases occur when

- p_b = 1,500 psia, permeability = 50 md.
- p_b = 2,000 psia, permeability = 50 md.
- p_b = 2,500 psia, permeability = 50 md.

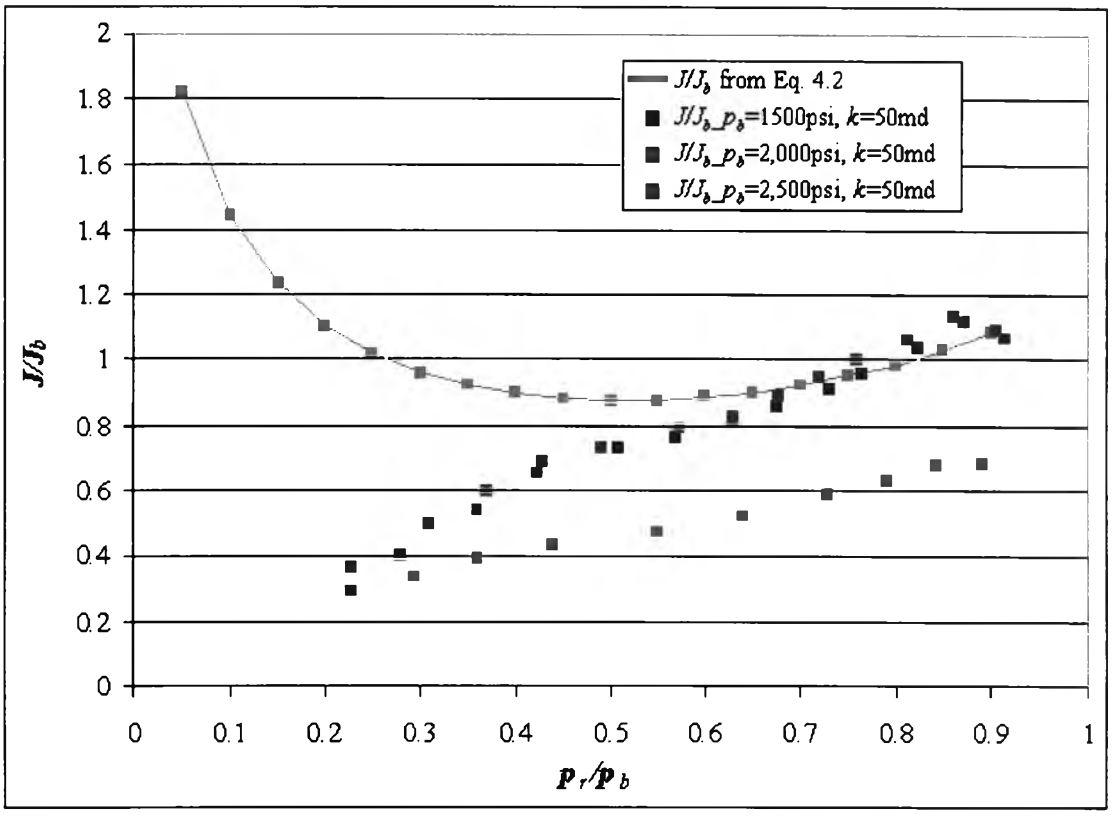

Figure 4.34: J/J_b value as a function of p_r/p_b which has different shape from calculation value of J/J_b.

Therefore, for the cases mentioned, there would be large error in the prediction of the values of n and J.

4.4 Sample Calculation of Future IPR.

This section illustrates sample calculation of future IPR which can be done in a step-by-step procedure as follows:

Step 1. From multipoint flow test for base case data, we obtain n = 1.0207 and J = 0.0085 at p_r = 1,588 psia.

Step 2. Use Eqs. 4.1 and 4.2 to solve for n/n_b and J/J_b.

$$\frac{n}{n_b} = \frac{2.8089 + 81.5803\left(\frac{1588}{2000}\right)}{1 + 86.0795\left(\frac{1588}{2000}\right) - 2.7669\left(\frac{1588}{2000}\right)^2} = 0.9997$$

$$\frac{J}{J_b} = \frac{2.6687 + 2.9247\left(\frac{1588}{2000}\right)}{1 + 11.2741\left(\frac{1588}{2000}\right) - 7.7311\left(\frac{1588}{2000}\right)^2} = 0.9839$$

Step 3. Solve for constants n_b and J_b using the dimensionless values obtained in Step 2.

$$n_b = \frac{n}{n/n_b} = \frac{1.0207}{0.9997} = 1.0210$$

$$J_b = \frac{J}{J/J_b} = \frac{0.0085}{0.9839} = 0.0086$$

Step 4. The deliverability at below the bubble point can be determined from the variable n_b and J_b and the ratio n/n_b and J/J_b. At reservoir pressure 1,750 psia, the estimation of n and J can be determined as:

$n = n_b\ (n/n_b) = 1.0210 \times 0.9999 = 1.0209$

$J = J_b\ (J/J_b) = 0.0086 \times 1.0587 = 0.0091$

The calculated valued of parameter n and J from Step 4 is almost the same as parameter n and J from simulation as shown in Step 1.

Step 5. Use Eq. 2.7 to solve for the new $(q_o)_{max}$ at $p_{wf} = 0$ psi, the new absolute open flow potential is

$(q_o)_{max} = 0.0091\ (1750^2)^{1.0209} = 38{,}078$ BOPD

Step 4 and 5 can be repeated to estimate deliverability at other pressures. Table 4.1 is the results of the calculation at different reservoir pressures for the base case reservoir.

IPR can be estimated from Eq. 2.12 together with Step 1 to 5 and shown in Fig. 4.35.

Table 4.1: Calculation results from base-case data.

p_r, psia	n/n_b	n	J/J_b	J	Calculated $(q_o)_{max}$, BOPD
1,750	0.9999	1.0196	1.0587	0.0073	30034.1
1,500	0.9999	1.0196	0.9529	0.0066	19732.6
1,250	1.0014	1.0212	0.8949	0.0062	13072.6
1,000	1.0057	1.0256	0.8781	0.0061	8642.2
750	1.0154	1.0355	0.9090	0.0063	5653.4
500	1.0382	1.0587	1.0187	0.0070	3650.9
250	1.1098	1.1317	1.3249	0.0091	2450.6

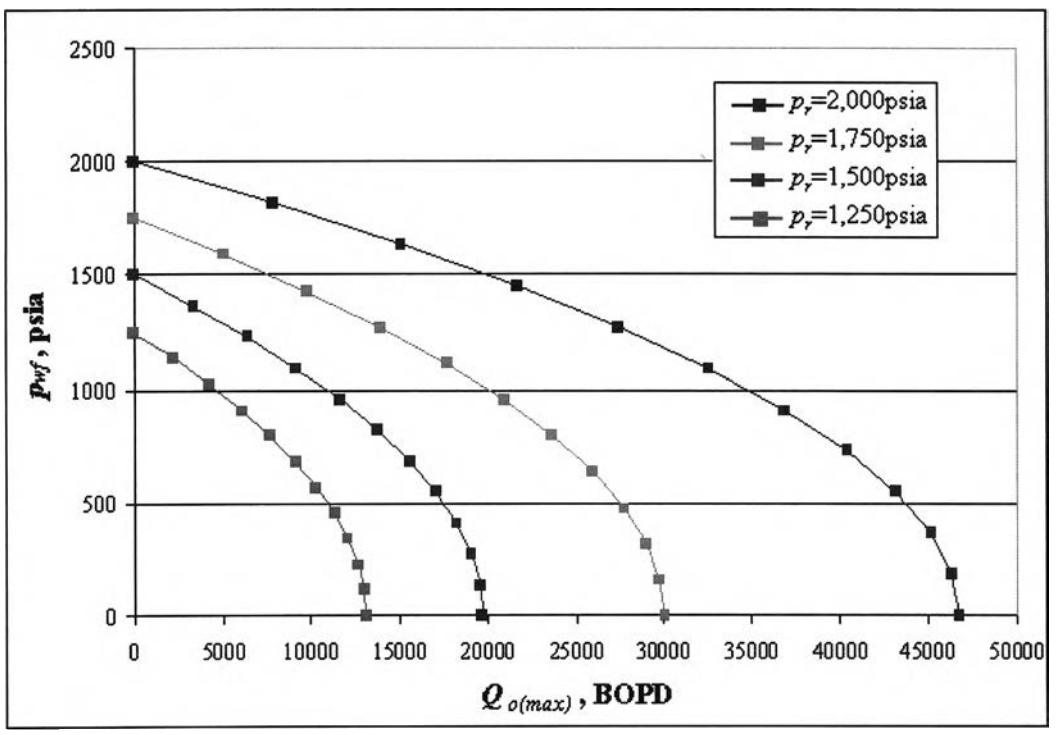

Figure 4.35: Base-case IPR curve.

4.5 Comparison of Future IPR.

Figs. 4.36 and 4.37 show the results of the predicted n and J values from Eqs. 4.1 and 4.2 vs. values from simulation, respectively. The values of n and J calculated from Klins and Clark equation are compared with values from simulation and shown in Figs. 4.38 and 4.39, respectively.

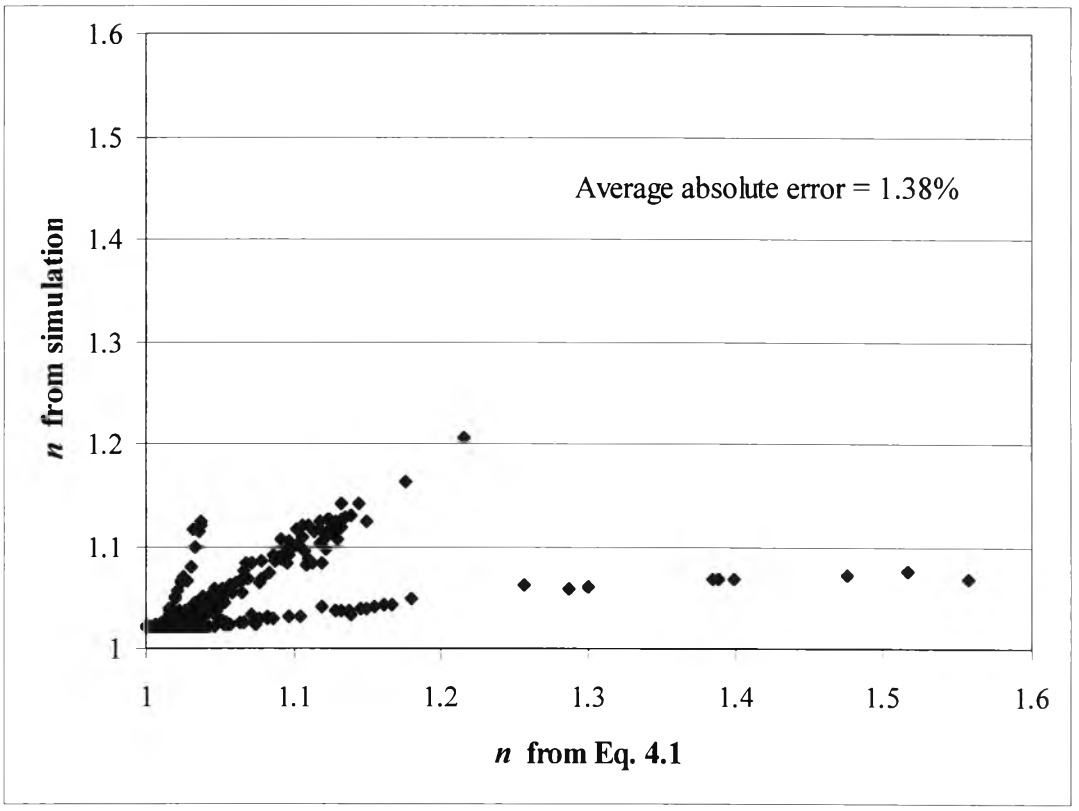

Figure 4.36: Error analysis of n value using the new approach.

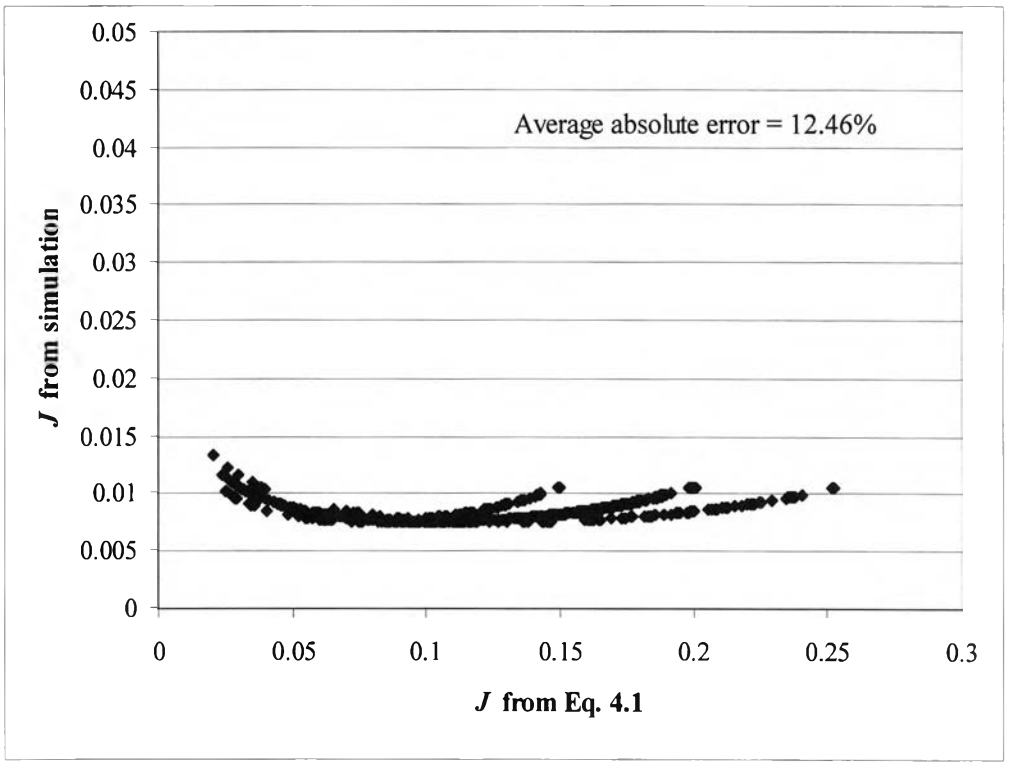

Figure 4.37: Error analysis of J value using the new approach.

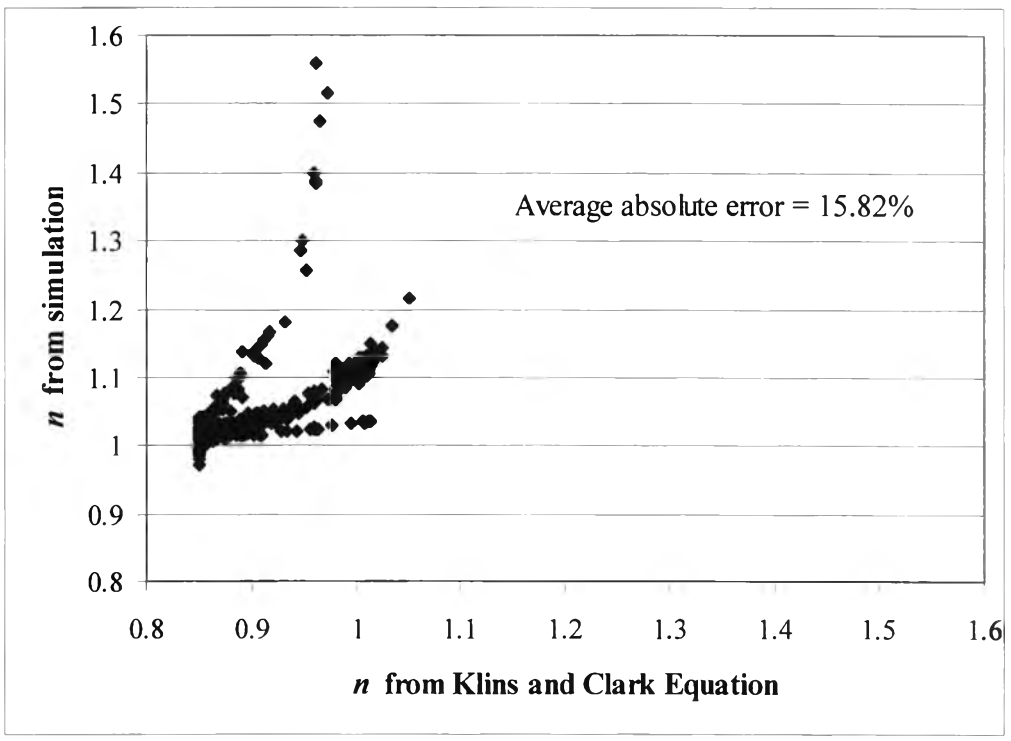

Figure 4.38: Error analysis of n value using Klins and Clark method.

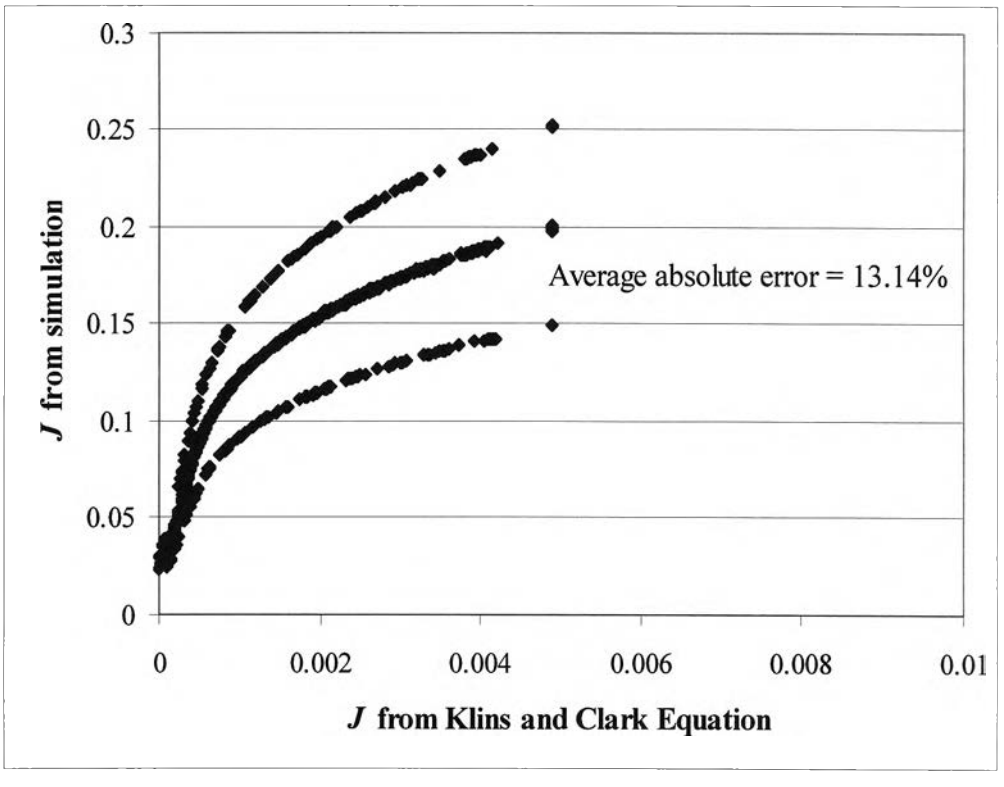

Figure 4.39: Error analysis of J value using Klins and Clark method.

From Figs. 4.36 to 4.39, the new approach yields a lower average absolute error between the actual results from simulation and prediction from empirical equations than the error between the actual results from simulation and the results from Klins and Clark equation.